Nuclear Instruments and Methods in Physics Research A 1059 (2024) 168973

Contents lists available at ScienceDirect

Nuclear Inst. and Methods in Physics Research, A

journal homepage: www.elsevier.com/locate/nima

Methods to maximize detector count rates on small-angle neutron scattering diffractometers at reactor sources: II. Optimizing sample, source and detector sizes

J.G. Barker

NIST Center for Neutron Research, National Institute of Standards and Technology, 100 Bureau Dr, Gaithersburg, MD 20899, USA

A R T I C L E I N F O

Keywords:
Neutron scattering
Small-angle scattering
Pinhole collimation
Diffractometer optimization
Diffractometer resolution
Detector layout
Nuclear reactor

A B S T R A C T

Methods for maximizing the detector count rate for the same scattering angle range and resolution are related to choosing the optimum pinhole collimation parameters which include the source and sample aperture sizes and collimation lengths on small-angle neutron scattering diffractometers located at reactor neutron sources. Calculations and experimental measurements are presented that show enhancements in count rate with the same q-resolution can be achieved by combining both longer flight paths with larger source and sample apertures and beam stop sizes. To be able to both accommodate the larger beam sizes at the detector and to maintain the same range in scattering angle, existing and new detector placement strategies are presented that extend the scattering angle range beyond what is capable with a single 2-D detector.

1. Introduction

Small-angle neutron scattering (SANS) diffractometers using pinhole collimation [1] typically have the source and sample apertures separated by a collimation distance L_1 and a detector located a distance L_2 after the sample aperture. To simplify the expressions, the sample is assumed to be located at the sample aperture. Typically, one two-dimensional (2-D) detector is placed on rails within a vacuum chamber to allow for ease in changing distance L_2 and is usually square having a pixel size ΔP. The beam is blocked by a beam stop slightly larger than the diameter of the beam D_B placed just before the detector. The entire path must be in vacuum to mitigate the background caused by air scattering. The collimation is shown schematically in Fig. 1. The collimation distance between the source and sample apertures L_1 is usually changed in discrete steps by neutron guide insertions after the helical neutron velocity selector (NVS) which chooses the mean neutron wavelength λ. In the first paper [2] we described the count rate optimization as related to the choice of wavelength λ. This second paper describes methods to maximize detector count rate as related to choices of both the source and sample aperture diameters D_1 and D_2 and the related beam path-lengths L_1 and L_2. The optimization methods for beam collimation used here are also described in Refs. [3–6].

The 2-D detector data is radially averaged where all centers of pixels having distance R in the range $R_i - \Delta R/2 \leq R \leq R_i + \Delta R/2$ are binned together in the same ith bin. The momentum transfer q corresponding to this bin is

$$q_i = \frac{4\pi}{\lambda} sin\left(tan^{-1}\left[R_i/_{L_2}\right]/2\right) \cong \frac{2\pi R_i}{\lambda L_2} \quad [1]$$

The detector count rate C_D collected in the ith bin is

$$C_D(q_i) = I_B d_s T_s \Delta\Omega_i \frac{d\Sigma}{d\Omega}(q_i) \quad [2]$$

where d_s and T_s are the sample thickness and transmission, respectively, I_B is the beam current incident on the sample, $\Delta\Omega_i$ is the solid angle of the detector annulus and $d\Sigma/d\Omega(q)$ is the macroscopic scattering cross-section of the sample. To minimize statistical errors from the number of counts on the detector, our goal is to maximize the detector count rate C_D collected over the same q range $q_i - \Delta q/2 \leq q \leq q_i + \Delta q/2$. The width of the annulus ΔR is typically chosen to be the pixel size ΔP when reducing the data: $\Delta R \cong \Delta P$. In our optimization calculations of detector count rate, we choose the annulus width ΔR_i such as to keep $\Delta q_i/q_i$ constant. Then the solid angle collected within the ith annulus is $\Delta\Omega_i = 2\pi R_i\ \Delta R_i/L_2^2 = \lambda^2 \Delta q_i q_i/(2\pi)$. Under these constraints and with fixed wavelength λ, the detector count rate is simply proportional to the beam current: $C_D \propto I_B$, with all other sample dependent parameters in Eq. (2) being fixed.

The beam brightness $P(\lambda)$ from the neutron moderator, has a strong

E-mail address: john.barker@nist.gov.

https://doi.org/10.1016/j.nima.2023.168973
Received 6 September 2023; Received in revised form 7 November 2023; Accepted 24 November 2023
Available online 29 November 2023
0168-9002/Published by Elsevier B.V.

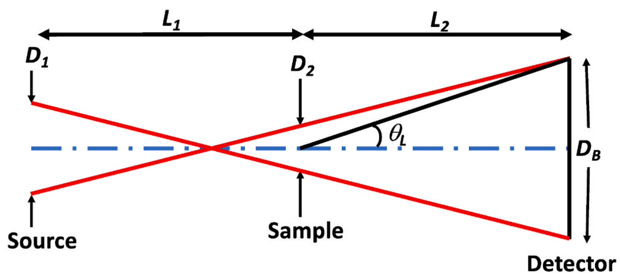

Fig. 1. Schematic of a pinhole SANS diffractometer's beam collimation.

dependence upon wavelength λ, but is nearly constant over area and the small divergence angle typically illuminated within the beam collimation. The beam current I_B on the sample follows the relation

$$I_B \cong \frac{\pi^2}{4^2}\frac{D_1^2 D_2^2}{L_1^2}T_G(L_1)\Delta\lambda P(\lambda) \propto \frac{T_G(L_1)D_1^2 D_2^2}{L_1^2} \quad [3]$$

where $\Delta\lambda$ is the wavelength band passed by the velocity selector, and the parameter $T_G(L_1)$ accounts for guide losses occurring during transport of the beam. The contribution to T_G from a single guide cut can be calculated using acceptance diagrams as presented in Fig. 9 from Ref. [7]. Measurements show that the correction T_G is close to unity, $0.8 \le T_G \le 1.0$, and is dominated by upstream gaps or cuts in the guide for the VSANS instrument used in this study [2,8].

In the next section we will add constraints such that the collimation parameters D_1, D_2, L_1, and L_2 can be chosen optimally.

2. Beam collimation optimization

For a SANS measurement, we need to measure over a q-range: $q_L \le q \le q_U$ where the subscripts L and U represent lower and upper limits, respectively. When optimizing the choice of possible instrument configurations, both the lower limit q_L or the q-resolution are possible constraints which we shall show produce very similar results. For q-resolution we use the variance $V_q(q)$, which is the square of the standard deviation $\sigma_q^2(q)$.

The lowest momentum transfer q_L is obtained from the radius of the smallest useable annulus R_L which must lie outside the beam stop and an additional distance to exclude any pixel partially obscured by the beam stop. The radius can be related to instrument parameters to be optimized by

$$q_L \cong \frac{2\pi R_L}{\lambda L_2} \cong \frac{\pi}{\lambda L_2}[\gamma D_B + \Delta R/2 + \Delta D/2] \quad [4]$$

where $\gamma \equiv B_S/D_B$ is the ratio of the beam stop diameter B_S to the maximum beam diameter D_B. It typically ranges around 1.1 to 1.2 and functions here as an enlargement factor to allow for beam stop misalignment. When choosing the minimum annulus radius R_L, the second and third terms, respectively, exclude any pixels partially shadowed by the beam stop by the annulus width ΔR and the detector spatial resolution full-width at half-maximum (fwhm) ΔD. For tube detectors, the detector spatial resolution is constrained to be within the tube diameter, and the stopping gas pressure is typically chosen so that along the tube axis the resolution ΔD approximates the tube diameter so that $\Delta R \cong \Delta D \cong \Delta P$. With other types of detectors, the pixel size can be significantly smaller than the spatial resolution, $\Delta P \ll \Delta D$. For example, at the NIST Center for Neutron Research (NCNR), the VSANS [8] diffractometer's high resolution scintillation detector has a pixel size $\Delta P = 0.080$ mm, which is an order of magnitude smaller than the spatial resolution $\Delta D = 0.85$ mm.

The beam size at the detector depends upon the collimation parameters as [5,9].

$$D_B \cong D_{B1} + D_{B2} = \frac{D_1 L_2}{L_1} + \frac{D_2(L_1 + L_2)}{L_1} \quad [5]$$

Gravity additionally expands the size of the beam profile only in the vertical direction and is often quite small. At the NCNR we use slightly oval shaped beam stops that have a vertical dimension 10 mm larger than the width, and thus block the vertically gravity-stretched beam profile while keeping the width unaffected.

For optimization purposes, the calculation can be greatly simplified by making some approximations. Typically, the contributions from gravity, the detector pixel size and spatial resolution are small and can be ignored. Then Eq. (3) can be rewritten substituting the fixed lower momentum vector constraint as $B_S = \gamma D_B$ and $q_L \propto B_S/L_2$ in Eq. (4) simply as

$$I_B \propto \frac{D_B^4 Y^2 (1-Y)^2}{L_2^2 \gamma^4 (1+X)^2} \propto \frac{q_L^4 L_2^2 Y^2 (1-Y)^2}{\gamma^4 (1+X)^2} \quad [6]$$

where $Y \equiv D_{B1}/(D_{B1} + D_{B2})$ and $X \equiv L_2/L_1$. Note the above relation is maximized with $Y = 0.5$, where the shape of the beam profile is similar to a cone and $D_{B1} = D_{B2}$.

Alternatively, q-resolution, expressed as the variance V_q in scalar q, can be used as the optimization constraint in place of the lower limit q_L, and is approximated as the sum of the variance in scattering angle V_θ and the variance in wavelength λ called V_λ as [3,5]

$$V_q = q^2\left[\frac{V_\theta}{\theta^2} + \frac{V_\lambda}{\lambda^2}\right] \quad [7]$$

By using the variance in angle V_θ as the constraint it can be shown that

$$I_B \propto \frac{V_\theta^2 L_2^2 Y^2 (1-Y)^2}{(1+X)^2 (1 - 2Y + 2Y^2)^2} \quad [8]$$

The parameters X, Y and V_θ in Eq. (8) are used to constrain D_1, D_2, and L_1. Note that Eqs. (6) and (8) are very similar simply by exchanging q_L^2 with V_θ. Both expressions are proportional to L_2^2. But to rescale the distance L_2 and keep all the other parameters fixed requires the simultaneous rescaling of D_1, D_2, and L_1, by the same factor. For example, doubling all four instrument parameters will cause the detector count rate to go up by a factor four through L_2^2, while X, Y, and V_θ all remain constant. The typical SANS diffractometer already takes advantage of this performance gain by having long flight paths and large aperture sizes when compared to pinhole SAXS diffractometers. Practical limitations on the source, sample and detector sizes guide the choices made in instrument design. Experimental measurements in the next section will test whether further gains can be achieved on the VSANS diffractometer at the NCNR by further enlarging collimation parameters.

The above expression is also proportional to $1/(1+X)^2$. Decreasing X thus also increases the detector count rate as shown both by calculation and measurement by Falcao [10]. To decrease X requires simultaneously increasing both the source size D_1 and the source-to-sample distance L_1 when comparing instrument configurations. Note that if the total flight path, $L_1 + L_2 =$ constant is used as an additional constraint, the revised optimization obtains the further constraint $L_1 = L_2$ [3]. This implies when designing a SANS instrument with constraints on the total flight path length, the maximum collimation distance L_1 and the maximum detector distance L_2 should be set to be equal. But for q-ranges where the detector is brought closer to the sample to reach larger scattering angles, then $L_1 > L_2$ can still be used, combined with larger source aperture D_1 to enhance the count rate.

Eqs. (6) and (8) differ slightly in terms of the Y parameter dependence and are plotted in Fig. 2. Both expressions predict maximum performance when $Y = 0.5$ where the source and sample apertures contributions to the beam size are equal. When Y is changed either smaller or larger than 0.5, the flat plateau or umbra region at the top of

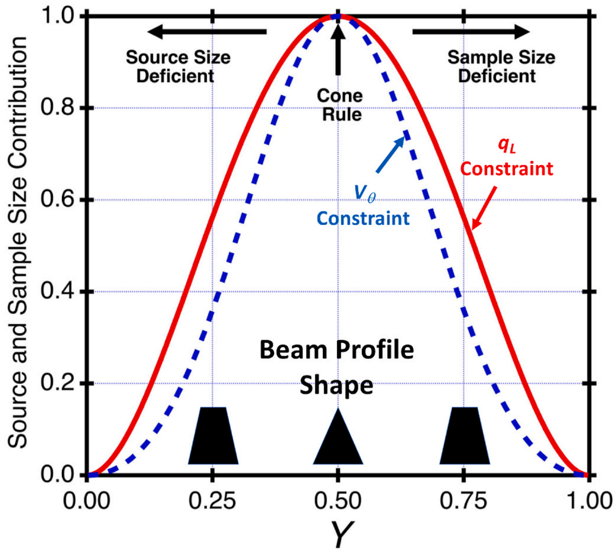

Fig. 2. Source and sample aperture contributions to Eqs. (6) and (8).

the beam profile grows in size. In practice constraints on available choices of sample and source sizes, and collimation and detector distances constrain the Y parameter to be either source size deficient with $Y < 0.5$ or sample size deficient with $Y > 0.5$.

Note the methods used here to derive Eq. (8) are the same as used by May [4] and Glinka [6], who both used the cone rule, which fixes $Y = 0.5$, to further constrain the final solution and thereby achieve a simpler expression. If we fix both X and Y in Eq. (8), it can be shown that $L_2 \propto L_1 \propto D_1 \propto D_2$ and $C_D \propto I_B \propto V_0^2 L_2^2$, which is equivalent to May's [4] Eq. (8) and Glinka's [6] Eq. (6). Both papers also use X to optimize the relationship between path lengths L_1 and L_2. The advantage of the current relations is the inclusion of the dependence of deviations from the cone rule provided by Y.

In practice we find that SANS diffractometers are configured routinely with Y significantly far from the ideal $Y = 0.5$, usually because the sample size is too small. Table 1 shows the instrument parameters for three instrument configurations that are commonly used together to cover a wide q-range from $q_L = 3.4 \times 10^{-3}$ Å^{-1} to $q_U = 0.6$ Å^{-1} on both 30m-SANS diffractometers at the NCNR [6] using a source aperture size $D_1 = 50$ mm and wavelength $\lambda = 6$ Å. The table also shows the impact of making the source size smaller ($D_1 = 25$ mm) or larger ($D_1 = 100$ mm). By simply adjusting D_1 and L_1 only, we can keep the q-range the same. Shrinking the available source size from 50 mm to 25 mm causes the count rate to be 0.69 times that of the original for all three configurations. The count rate losses are mitigated by adjustments in other parameters all within available ranges for the instrument and as calculated by Eq. (6). Expanding the available source size from 50 mm to 100 mm causes the count rate to be 1.23 times that of the original for all three configurations. But for the lowest q-range measurement, both the necessary flight path of $L_1 = 26.12$ m extends beyond the instrument's range, and the gravity term can no longer be safely ignored.

Increasing the instrument total length must be incorporated into the instrument design at an early stage and will significantly increase the instrument's cost. The maximum value is often limited by the size of the guide hall. The D11 diffractometer at the Institut Laue-Langevin (ILL) [11] has the longest total path length of $L_1 + L_2 = 80$ m for any currently operating SANS pinhole diffractometer. The strength of the gravity term quickly gains significance at the longest instrument setting and at longer wavelengths and should be included in any final optimization determination. With more common instrument lengths of 20 m–40 m and shorter typical wavelengths $\lambda \leq 6$ Å, the gravity term remains small in comparison to the dominant aperture terms. For an existing instrument having fixed total length in this range, very significant gains in count rate can be obtained when replacing current instrument configurations at an intermediate q-scale which utilize less than the full path-length of the instrument with configurations where all the size parameters can now be increased simultaneously.

The maximum sample aperture size is usually quite easy to expand on most diffractometers. But increasing the sample size and accompanying ancillary sample environments beyond current typical sizes of 10–20 mm can be more difficult and costly. If the sample thickness is kept constant, the volume of sample required will scale as D_2^2. The cost to experimenters can be considerable for some deuterated materials. Some magnetic single crystals cannot be grown as large as even the current optimal size. Significantly increasing sample volume may also be costly in time or money for samples requiring extensive laboratory preparations particularly for biological systems. Most of the sample environments used on SANS diffractometers, such as rheometers [12], cryostats, or magnets are designed with a maximum sample size consideration. Some neutron instruments are designed to use much larger sample sizes, particularly for temperature-controlled liquid samples. Fig. 3 shows four types of demountable sample cells available at the NCNR designed to hold liquid, having fill diameters of 19 mm, 28 mm, 40 mm, and a rectangular geometry having a 38 mm by 76 mm area. The 40 mm diameter cell is used on the Neutron spin echo (NSE) at the NCNR, and the largest rectangular cell is used to cover 18 converging beam option on the VSANS instrument [8]. The cells fit into temperature control blocks that cover the temperature range from −10 C to 250 C.

The maximum source size is usually limited to the dimensions of the rectangular neutron guide connecting the instrument to the neutron source. The guide size in principle is only limited by the size of the cold moderator, but in practice is also limited by sharing the viewing area

Table 1
The first three rows are collimation parameters for the three configurations most used together to cover an extended q-range on both 30m-SANS diffractometers at the NCNR using source aperture size $D_1 = 50.8$ mm, wavelength $\lambda = 6$ Å and detector pixel size $\Delta P = \Delta D = \Delta R = 5.08$ mm. Also included are hypothetical configurations using both smaller ($D_1 = 25$ mm), in rows 4–6, and larger ($D_1 = 100$ mm), in rows 7–9, source apertures and where L_1 is adjusted to match the beam size. The column labeled # corresponds to the instrument configuration with subscript corresponding to size of D_1. The last column is proportional to the beam current I_B. Configurations covering the same q-range produce a loss of −31 % with smaller source aperture $D_1 = 25$ mm while a gain of +22 % is achieved if source aperture size is increased to $D_1 = 100$ mm when compared to equivalent configurations having $D_1 = 50.8$ mm.

#	q_L (Å^{-1})	L_1 (m)	L_2 (m)	D_1 (mm)	D_2 (mm)	B_S (mm)	D_{B1} (mm)	D_{B2} (mm)	D_B (mm)	γ	X	Y	$D_1^2 D_2^2 / L_1^2$ (mm^2)
1_{51}	3.40×10^{-3}	14.72	12.50	50.8	12.7	76.2	43.1	23.5	66.6	1.14	0.849	0.648	1.92×10^{-3}
2_{51}	7.31×10^{-3}	8.52	4.00	50.8	12.7	50.8	23.9	18.7	42.5	1.20	0.469	0.561	5.73×10^{-3}
3_{51}	2.20×10^{-2}	3.87	1.33	50.8	12.7	50.8	17.5	17.1	34.5	1.47	0.344	0.506	2.78×10^{-2}
1_{25}	3.40×10^{-3}	8.73	12.50	25	12.7	76.2	35.8	30.9	66.6	1.14	1.432	0.537	1.32×10^{-3}
2_{25}	7.31×10^{-3}	5.06	4.00	25	12.7	50.8	19.8	22.7	42.5	1.20	0.791	0.465	3.94×10^{-3}
3_{25}	2.20×10^{-2}	2.30	1.33	25	12.7	50.8	14.5	20.0	34.5	1.47	0.578	0.419	1.91×10^{-2}
1_{100}	3.40×10^{-3}	**26.12**	12.50	100	12.7	76.2	47.9	18.8	66.6	1.14	0.479	0.718	2.36×10^{-3}
2_{100}	7.31×10^{-3}	15.11	4.00	100	12.7	50.8	26.5	16.1	42.5	1.20	0.265	0.622	7.06×10^{-3}
3_{100}	2.20×10^{-2}	6.87	1.33	100	12.7	50.8	19.4	15.2	34.5	1.47	0.194	0.561	3.42×10^{-2}

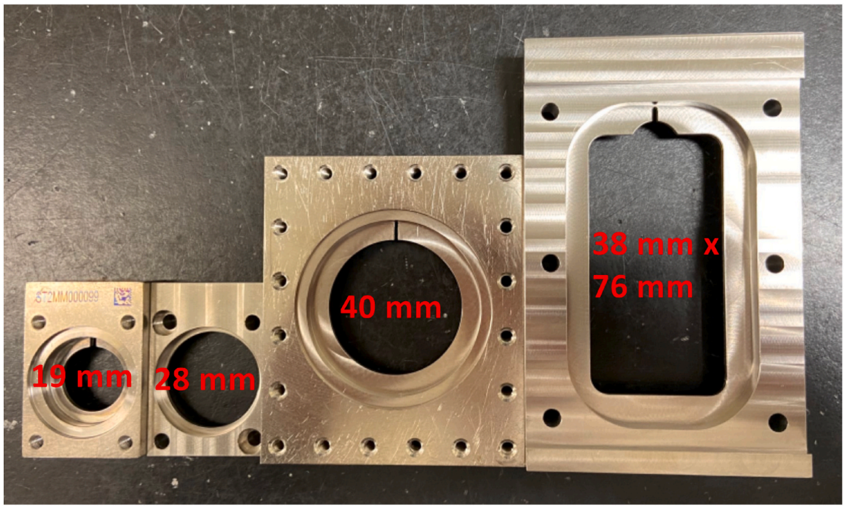

Fig. 3. Different size cells for liquid samples available at the NCNR with diameter of fill volume indicated.

with neighboring rectangular guides with different incident viewing angles. At the NCNR the moderator is viewed through an elliptical window having a width of 150 mm and height of 200 mm, allowing the rather large 60 mm wide × 150 mm tall NG-3 guide for the VSANS diffractometer. The guide width could in principle be increased further to 100 mm, but produces other engineering challenges for the redesign of other instrument components such as enlargement of NVS, polarizing cavities, *etc*.

The above optimization can also be applied to SANS diffractometers that utilize time-of-flight (TOF) for wavelength determination. But the pulse frequency is fixed by the pulsed spallation source, which constrains the overall instrument length from source to detector to avoid frame overlap, which can limit the accessible wavelength range. For TOF diffractometers located at reactor sources [13,14] the pulse frequency is independently controlled by the disk choppers and thus do not have the additional frame overlap restrictions on instrument length.

To reiterate, a significant gain in count rate can be achieved utilizing either of the above optimization constraints Eq. (6) or 8 by enlarging simultaneously 2-D detector size, both apertures, beam stop, and both path lengths: R_U, D_1, D_2, B_S, L_1 and L_2. Currently the most difficult parameter to enlarge is the maximum annulus radius, R_U which is typically limited by the maximum size of the 2-D detector. Alternatively, additional detectors can be placed closer to the sample to expand the angular range covered. Current and proposed detector layouts to extend the effective limitation on detector size are discussed in the fourth section.

3. VSANS performance test using large samples

SANS measurements were made on the VSANS diffractometer to test the calculated gains in instrument performance. The instrument has three detector carriages that can be placed at variable distances. The rear carriage with the high-resolution detector was not used. The middle and front carriages each contain four detector panels, with each panel having an adjustable distance from the beam center. The gap between the left and right panels on the middle carriage was minimized to make a single detection region 0.8 *m* wide by 1.0 *m* tall. Front carriage openings between the panels were adjusted to allow passage of the scattered beam to the middle carriage. Three instrument configurations were chosen such that the *q*-range was identical, but the sample aperture size D_2, distances L_1, L_2 and beam stop size B_S were varied as listed in Table 2. For the measurements, a 100 mm × 100 mm sheet of PTFE or cheese were used. By placing the front carriage at fixed distance $L_2 = 3.78\ m$ and panel opening of 150 mm wide × 180 mm tall, the same maximum $q_U = 0.15$ Å^{-1} was measured for all three configurations. Fig. 4a plots the background corrected and absolutely scaled scattering cross-section, by the method described by Kline [15]. By comparing the sum of the detector count rates from all detector panels, the gain in performance was estimated. Doubling the sample aperture size from $D_1 = 11$ mm–22 mm, increased the calculated count rate by a factor of 3.0. Increasing the sample aperture size further to 38.1 mm produced a total gain in detector count rate of 5.7. The observed gains in count rate are listed in Table 3, and most closely match the calculated values according to Eq. (3).

The lower *q* limit is nominally the same for all three configurations if the effect of the detector spatial resolution is ignored. Table 2 calculates that the smallest beam stop has a *q* limit corresponding to only 16 % larger than the largest beam stop. But inspection of the scattering curves in Fig. 4a shows that the downturn caused by the smallest beam stop begins at significantly higher *q* than that calculated in the table. Possibly the contribution of the detector spatial resolution is underestimated. The smallest sample and beam stop sizes correspond to typical use of the instrument. Thus, the largest sample produced both a gain in count rate of 5.7 and a smaller *q*-limit over the typical case.

Note the three instrument configurations as chosen in this measurement do not all maximize the *q*-range covered. As shown in Fig. 4b, the front carriage's detector panels partially block the middle carriage's detector panels' view. The *q*-range for the $B_S = 5$ cm and 10 cm cases

Table 2
Collimation parameters for three configurations of the rear detector carriage used on the VSANS instrument to test the performance using larger sample and beam stop sizes. The minimum momentum transfer q_L is calculated using $\lambda = 8$ Å and detector pixel size $\Delta_P = 8.0$ mm. The gain G in beam current is calculated using Eq. (3) with respect to the first instrument configuration.

q_L (Å^{-1})	L_1 (m)	L_2 (m)	D_1 (mm)	D_2 (mm)	B_S (mm)	D_{B1} (mm)	D_{B2} (mm)	D_B (mm)	γ	X	Y	G
3.77×10^{-3}	13.59	6.95	60	11.1	50.8	30.7	16.8	47.4	1.072	0.511	0.648	1.0
3.40×10^{-3}	15.60	13.61	60	22.2	102	52.3	41.6	93.9	1.082	0.872	0.557	3.04
3.26×10^{-3}	19.54	20.28	60	38.1	152	62.3	77.4	139.9	1.089	1.038	0.445	5.70

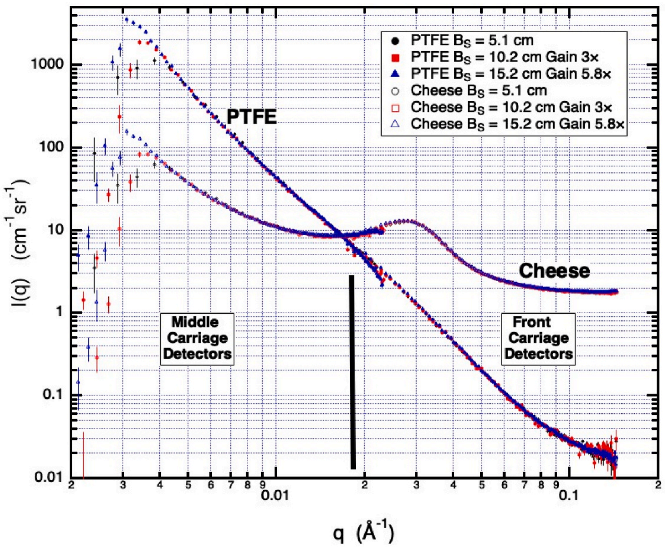

a

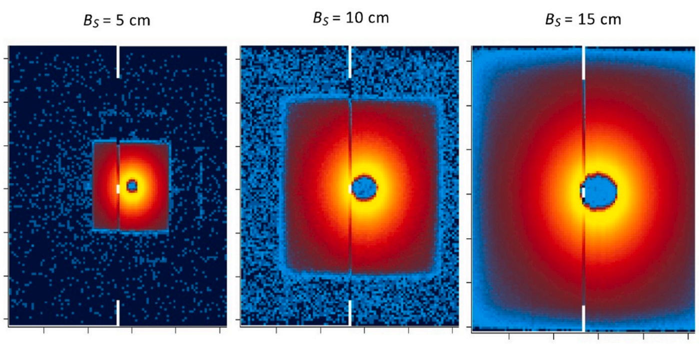

b

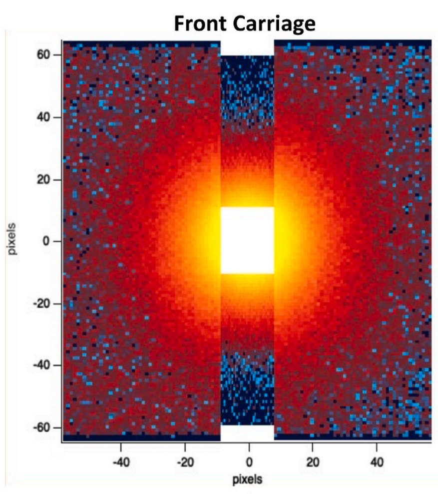

c

Fig. 4. Panel a) Scattering cross-section from poly (tetrafluoroethylene) (PTFE) measured on the VSANS instrument over the same q-range but with different size sample apertures and beam stops as given in Table 2. Panel b) Middle carriage 2-D detectors' images from PTFE sample from the three instrument configurations. Panel c) Front carriage 2-D detectors' image.

Table 3
The observed ratio in detector count rates between the second, $B_S = 102$ mm, and third, $B_S = 152$ mm, instrument configurations with respect to the first configuration, $B_S = 51$ mm, as observed for the two different samples and on the two different detector carriages. The configurations' details are listed in Table 2.

Sample	B_S (mm)	Front	Middle
PTFE	102	2.99	3.12
Cheese	102	2.98	2.83
PTFE	152	6.38	8.60
Cheese	152	6.22	6.06

could have been extended to larger q by moving the front carriage closer to the sample. If there was not a second detector, which is the case at most facilities, the q-range would also be largest with the smallest beam stop $B_S = 5$ cm. Alternative detector designs are presented in section 4 that allow an extension of the q-range to mitigate this affect.

4. Alternate detector designs to extend q-range

This section will explore detector geometries that can most economically cover a larger scattering angle range with nearly full azimuthal coverage. SANS measurements usually require data to be collected over as wide of a q-range as possible. TOF measurements allowing a large wavelength range $\lambda_L \leq \lambda \leq \lambda_U$ as commonly done at Spallation neutron sources [16–20] and at reactors using disk choppers [13,14] already extend the q-range by the ratio λ_U/λ_L. Since we wish to increase θ_U, we need to find alternative methods to either increase R_U or decrease L_2.

The types of detector geometries that can extend scattering angle range can be broken down into three general categories: i) increasing the size of the 2-D detector placed on the rear carriage, ii) placing additional 2-D detectors at a few intermediate distances or iii) a new concept of using fixed 1-D tubes spaced along the flight path to provide full solid angle coverage. Each category will be discussed separately. Each detector will be constructed from 1-D detector tubes filled with ^{3}He gas.

Factors that typically affect the detector performance are count rate capability, background per unit of solid angle, spatial resolution ΔD and pixel size ΔP. The total cost often scales linearly with detector area when using the same components. But the cost can be mitigated by increasing the size of some detector components as a function of the scattering angle. The count rate per solid angle is usually several orders of magnitude higher at the smallest versus the highest angle of a measurement. For this reason, the detector components at small angle need higher count rate capability but may tolerate higher detector background when both are scaled by solid angle. Improving the spatial resolution usually also increases the cost per unit area by increasing the number of electrical components among other technological factors. The maximum count rate per tube should be kept below some value to avoid spatial distortions, which is found to be 10,000 s^{-1} for the VSANS instrument [8]. If the expected count rate will exceed this value, strategies that either increase the number of tubes or use other detector technologies that can handle higher count rates should be considered.

4.1. Larger rear 2-D detector

Larger 2-D detectors can be built to compensate for the larger beam stop or otherwise extend the θ-range. Current trends in SANS diffractometer design have produced somewhat larger detectors of 1 $m \times 1$ m area than earlier designs using 1 m long and 8 mm diameter tubes filled with ^{3}He [21,22]. The largest current rear detector on a SANS diffractometer is on TAIKAN at Japan Proton Accelerator Research complex (J-PARC) [17], which uses 8 mm diameter tubes to produce a detection area of 2.1 m $\times$ 2.1 m.

Both the spatial resolution and pixel size normally needs to be smaller at smaller angles to improve q-resolution. If spatial resolution and pixel size nearly match, $\Delta D \cong \Delta P$, then to keep the detector contribution to the variance smaller than 1/4 of the beam contribution requires $\Delta D \leq D_B/4$ near the beam stop. Thus, we choose our minimum beam stop size to be $B_S \geq 5 \times \Delta D$.

At the outer regions of the detector the wavelength contribution dominates, which allows us to use a larger size in this region: $\Delta D \leq (R_i/2)\Delta\lambda/\lambda$. This constraint allows us to use larger diameter tubes when adding additional detector coverage beyond the central detector, and thus reduce the total number of tubes and subsequently cost. At reactor sources where wavelength selection is obtained using a NVS with rather broad wavelength spread having 10 % < $\Delta\lambda/\lambda$ < 20 %, even larger area detectors can be created using larger diameter tubes for the outer regions without a reduction in q-resolution. This will reduce the number of tubes needed considerably and thus lower the cost. For example, the LET instrument at the ISIS Neutron and Muon Source uses ^{3}He filled tubes of 25 mm diameter that are 4 m long having $\Delta D = 25$ mm [23]. There will be a significant additional cost for a larger diameter vacuum chamber needed to house the much larger rear detector.

4.2. Second detector carriage

If the rear detector distance can be adjusted by use of rails, the addition of 2-D detectors at intermediate distance also need to be placed on rails. The D33 TOF SANS diffractometer at the ILL [13], the BILBY SANS diffractometer at the Australian Nuclear Science and Technology Organization (ANSTO) [14], and the VSANS diffractometer at the NCNR [8] use four 2-D detectors mounted on a second carriage on rails. This detector bank is placed closer to the sample and individual lateral positions are adjustable to form a rectangular opening of adjustable size. This combination of two detector carriages provides an adjustable method to choose the angular range. Full coverage of the scattering solid angle between the scattering angle limits $\theta_L \leq \theta \leq \theta_U$ is achievable in this arrangement. By altering the opening size and carriage distance, these instruments have added flexibility in the range of scattering angle covered. SANS diffractometers at spallation neutron sources have often used fixed detectors placed at intermediate distances to cover the entire angle range without need for any position adjustment [17–19]. A second 2-D detector is sometimes placed at a closer distance and shifted laterally to one-side to reach higher angles with partial azimuthal angle coverage [21].

A significant disadvantage of placing the detector closer to the sample is the increase in the sample contribution to the angular resolution. This may limit the maximum angular range that can be achieved. For intermediate angular range the wavelength contribution normally dominates the angular component. The example calculation in section 4.4 will show the angular dependence for a magnification of five.

4.3. Spaced tubes lining detector vessel

Another new approach to reduce the detector area is to space the tubes along the length of the vessel. The general layout is similar to an early design proposed for LOKI at the European Spallation Source (ESS) [24]. Four tubes are placed in a square group arrangement as shown in Fig. 5. Pairs of vertically oriented 1-D tube detectors lie on the left and the right side, each placed one tube diameter closer to the sample than the top and bottom tubes. Each subsequent detector group is positioned a distance closer to the sample that allows an unobscured view of sample. The spacing between groups steadily decreases as the scattering angle increases. Thus, any four-tube group at a given distance provides full 2π azimuthal coverage, and all the groups together provide full solid angle coverage within the covered scattering angle range. This approach has several advantages. The tube coverage can be extended to cover a larger scattering angle range, removing the need to move any 2-D detectors along rails or laterally. The rear 2-D detector can remain fixed at the maximum distance. A larger tube diameter can be chosen such that the resolution is still always limited by the wavelength term, reducing

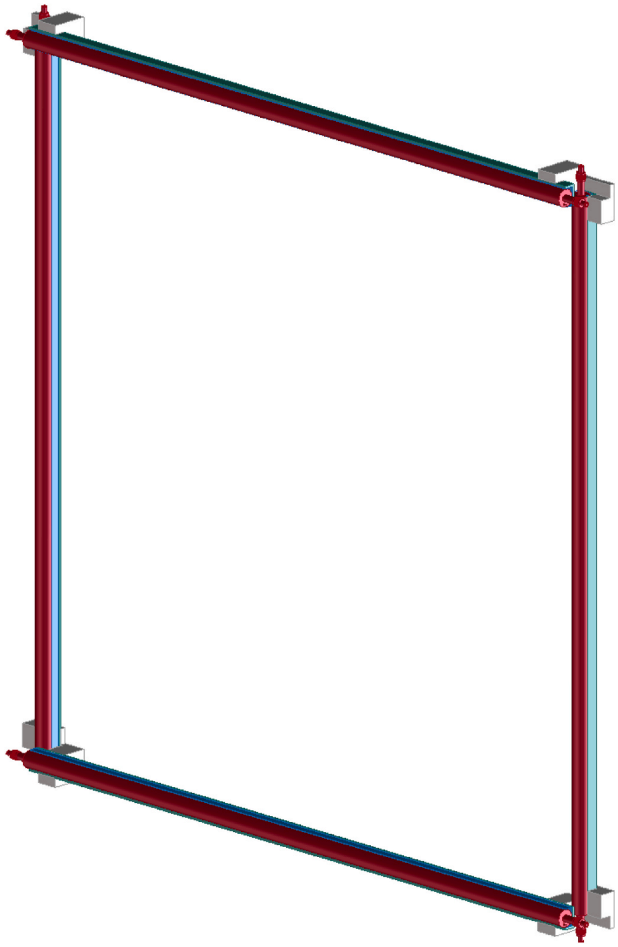

Fig. 5. Schematic of one group of four 40 mm diameter and 1 *m* long 1-D detector tubes used to construct the spaced tube lining detector. Three-sided neutron shield is removed for clarity.

the number of tubes needed. The growth in the sample term of V_θ is also mitigated by the larger overall distance from the sample for many of the tube groups when compared to intermediate distance 2-D detectors. By wrapping the tubes in a three-sided neutron shield that is only viewed from the sample, the background from backscattering from the tube shell can be shielded from all the other detector groups. In this way, any backscattering from the vessel lining should be eliminated. Such back-scattered background has recently been observed on both the 30m-SANS and VSANS diffractometers at the NCNR [25].

Placing tube detectors inside a vacuum presents some design challenges. The electronics' performance and long-term survival depends upon maintaining temperature within an acceptable range without overheating. We plan on using filtered air flow through periodically placed air boxes inside the vessel that contain the electronics for cooling. The high voltage applied to the tube end connections must also be either kept in air inside hermetically sealed tubing [21] or in vacuum with pressure less than 0.1 Pa [8] to prevent Corona discharges from destroying the electronics.

4.4. Resolution calculation comparing detector layouts

Four different practical detector concepts to extend the *q*-range a factor of five beyond the range obtained using a 1 m × 1 *m* rear detector is presented. The detectors utilize only ^{3}He tube 1-D detectors of different diameters and lengths. All four concepts utilize the same rear detector to cover the angular range 0 Rad $\leq \theta \leq$ 0.025 Rad (1.43°) placed at $L_2 = 20$ *m* having 112 tubes each having 8 mm diameter and 1.0 *m* active length to make a 1.0 *m* × 1.0 *m* detection region, like several existing SANS detectors [21,22]. The spatial distribution of the different detector concepts is presented in Fig. 6. If η is the expansion in the angle covered, the extended detector areas A_{ex} scale as Concept 1) larger area detector: $A_{ex}/A_R \propto \eta^2$-1, Concept 2) intermediate distance arrays: $A_{ex}/A_R \propto (\eta^2\text{-}1)\,(L_{2F}/L_{2R})^2$ or Concept 3) spaced tubes: $A_{ex}/A_R \propto 2 \times \ln(\eta)$, where subscripts R and F refer to rear or front detectors, respectively.

For the Concept 1, a single carriage is used to hold a much larger area detector, with the inner 1 m × 1 *m* region being as described above, and with an added outer detection region of 5 m × 5 *m* surrounding the central detector at $L_2 = 20$ *m*. In terms of cost, this option is the least practical, but has a small advantage in having better angular resolution. On each side are placed 100 tubes having 40 mm diameter and 2.5 *m* length, with two tubes placed in line to cover a total 5 *m* length, and above and below are placed 50 tubes having 1.0 *m* length placed horizontally to fill the gaps between the left and right panels. Note that both ends of a tube have a dead space where neutrons are not detected, and additional space is needed for an electrical connector. Thus, a small detector dead area will exist between the two vertically aligned tubes.

For Concept 2, to extend the *q*-range this uses a front carriage having four 2-D panels as used on the VSANS diffractometer located at $L_{2F} = 4.0$ *m*. The panels have a separation of 85 mm between left and right panels and top and bottom panels to allow the lower angle scattering to pass unimpeded to the rear detector.

For Concept 3, there are forty groups of four tubes spaced in distance from the detector 0.96 m $\leq L_2 \leq$ 20 *m*. The tubes have 1.08 *m* length and 40 mm diameter with the tube axis placed 0.52 *m* from the optic line of sight created by the two apertures. Concept 4 is like Concept 3 except that the tube diameter is reduced from 40 mm to 8 mm to improve detector spatial resolution. This requires the number of group positions needed for complete coverage to increase from 40 to 200 for a total of 800 detectors.

The angular range covered by the first two concepts extends a factor

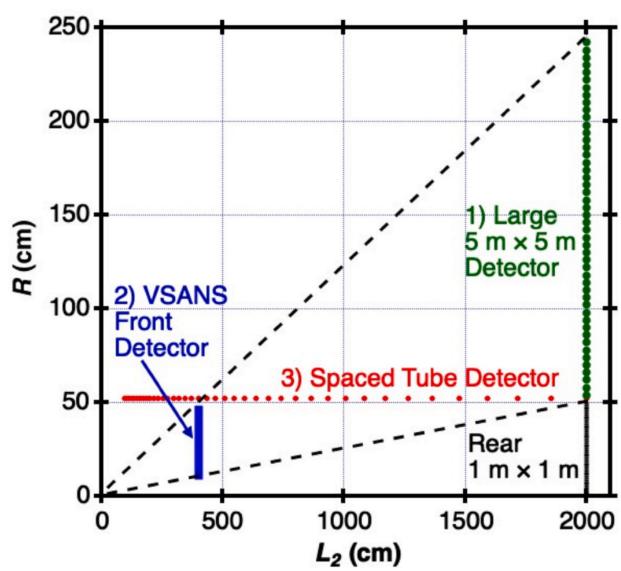

Fig. 6. Horizontal section at beam height showing right half of three types of extended angle detectors: 1) Large 5 m × 5 *m* detector at $L_2 = 20$ m (green), 2) VSANS right panel on front detector at $L_2 = 4$ m (blue), and 3) spaced tube detector using 40 mm diameter tubes (red). Angles between dashed lines show angle range covered by 1) and 2).

of five farther than the 1 m × 1 m rear detector, from 0.025 Rad (1.43°) ≤ θ ≤ 0.124 Rad (7.13°), while the third and fourth concepts extend a factor of twenty farther, from 0.025 Rad (1.43°) ≤ θ ≤ 0.124 Rad (28.4°). Concept 2 can be extended to cover the full angular range gain of twenty by adding a third carriage with similar four detector panels with distance $L_2 = 1.0\ m$. With the addition of a third array of detectors, the positions could be fixed like some spallation source SANS diffractometers. Expanding the angular range of concept 1 to a factor of 20 is not feasible.

To achieve the same detector efficiency, 40 mm diameter tubes are filled with a pressure of ^{3}He of 0.16 MPa (1.6 bar), which is 1/5 the pressure of 0.8 MPa (8 bar) needed for the 8 mm diameter tubes. Subsequently, the amount of ^{3}He gas needed simply scales with the total detection area. Table 4 lists the size and number of each type of tubes, and the detection areas for each concept. The total number of tubes for the first three concepts are similar. But the detection area differs sharply, with the smallest area needed for concept 2.

The variance of the q-resolution as a function of q is plotted in Fig. 7, for two different collimation settings available on the VSANS at the NCNR as described in Table 5. The dashed lines in the three panels correspond to only the wavelength contribution to the variance, each corresponding to a different monochromator (highly-oriented pyrolytic-graphite (HOPG): $\Delta\lambda/\lambda = 1$ %; NVS: $\Delta\lambda/\lambda = 12.5$ %; and deflector: $\Delta\lambda/\lambda = 44$ %). The symbols represent the sum of the angular and wavelength contributions to the variance for every tenth tube. For the best overall q-resolution obtained using HOPG wavelength selector and the tightest collimation option, the spaced tubes Concept 4 with 8 mm diameter tubes is the most appropriate choice. Since the sample aperture component to the resolution $V_{\theta 2}$ is weighted by $(L_1+L_2)^2/L_2^2$, the two-carriage Concept 2 generally has the poorest angular resolution performance. But wavelength resolution is still the dominant contribution for all four concepts whenever using the deflector ($\Delta\lambda/\lambda = 44$ %), and for all except a small q-range of the two carriage Concept 2 when using the NVS ($\Delta\lambda/\lambda = 12.5$ %).

The four presented detector concepts were developed to be practical to build. Concept 2 using two carriages is the version built at the VSANS at the NCNR. It was chosen to reduce the cost, and the ability to simply add a third carriage containing a higher resolution detector for higher resolution measurements. Concept 4 using spaced tubes with 8 mm diameter was briefly considered at an early stage of design for the VSANS because it provided the necessary angular resolution when using HOPG, but was deemed too costly, especially considering the high price of ^{3}He at the time. A proposed upgrade to one of the 30m-SANS instruments that uses a NVS will utilize Concept 3. The ability to cover a wider angular range without moving detectors is seen as a key advantage of Concept 3 over 2. Concept 1 using a larger single carriage detector can be built based on similarities to the LET detector at ISIS [23] which uses 384 1-D ^{3}He tube detectors having 25 mm diameter and 4 m length, with area coverage of 38.4 m^2. The larger number of tubes and ^{3}He gas, combined with the larger vacuum vessel makes this the most expensive option with similar resolution to Concept 3.

Table 4
Parameters used to describe the four detector concepts for extended q coverage.

Parameter	1) 5 m × 5 m Rear Detector	2) VSANS Second Carriage	3) Spaced Tubes 40 mm dia.	4) Spaced Tubes 8 mm dia.
Angular Range: θ_L-θ_U	0.025–0.124 Rad	0.025–0.124 Rad	0.025–0.50 Rad	0.025–0.50 Rad
Tube Detectors $L_t \equiv$ length $N_t \equiv$ number	40 mm diameter $L_{t1} = 2.5\ m$ $N_{t1} = 200$ $L_{t2} = 1.0\ m$ $N_{t2} = 100$	8 mm diameter $L_{t1} = 1.0\ m$ $N_{t1} = 96$ $L_{t2} = 0.5\ m$, $N_{t2} = 96$	40 mm diameter $L_t = 1.0\ m$ $N_t = 160$	8 mm diameter $L_t = 1.0\ m$ $N_t = 800$
Detector area	24 m^2	1.15 m^2	6.4 m^2	6.4 m^2

5. Discussion

The previous sections have shown that the detector count rate can be increased by enlarging different length scales of the instrument. This section will discuss other details that may affect the decisions to use such features, both involving the final data accuracy and practicality.

Signal-to-noise (S/N): Our goal can be defined as measuring the scattering curve on an absolute scale over a set q-range and q-resolution to a set accuracy in the minimum amount of time. By increasing the count rate, we can measure the same signal in less time. But we must also consider the effect on the S/N ratio which also affects the accuracy. When making this comparison, both the signal and the noise should be scaled by the same solid angle on the detector [8]. The signal will then scale directly with beam current on sample. The noise can scale differently depending on the detector configuration, for example.

The background or noise for SANS measurements typically are measured in two separate background measurements: a blank sample, that can be either an empty, solvent or other sample holder and a blocking material that stops the beam at the sample position. The background can be typically broken into several components: i) a dark current that comes from sources independent from the beam on sample, ii) parasitic halo around the beam stop that originates from the beam collimation and iii) background scattering originating from the blank sample, holder and surrounding environment. Both ii) and iii) scale directly with beam current while i) is largely independent of beam current on sample. In most cases ii) and iii) are dominant keeping the S/N constant when comparing changes in instrument configuration affecting beam current. With constant S/N, the counting time needed for constant data accuracy scales inversely with the detector count rate. Thus, if the count rate doubles the counting time needed is halved.

But in cases where the dark current i) is dominant, the noise is independent of the signal. The dark current is largely proportional to detector area, and originates from either nearby instruments, or is from cosmic rays, that all penetrate the shielding around the vessel to reach the detector. Measurements of the dark current on the detectors at the NCNR SANS diffractometers is found to remain roughly constant regardless of the distance from the sample. Thus, more compact or shorter instruments with smaller detector areas will lower this noise component as $N \propto L_2^2$. This may occur when iii) has been successfully minimized, such as using high q-resolution which lowers the beam current, using vacuum to eliminate air scattering, and samples having low intrinsic background such as being hydrogen free.

Lens Focusing: In the case of a perfect lens optical device that does not have aberrations in the image, the sample aperture term is eliminated, $D_{B2} = 0$, allowing any sample size to be used without impact on q-resolution or q-range. If the sample size is constrained, a lens can enhance the beam current by four for the same q_L and two for the same σ_q [26]. Much higher gains can be achieved by allowing the sample size to be increased. For example, using a lens to focus the high-resolution configuration in Table 5 allows the source size D_1 to be increased from 15 mm to 30 mm to maintain q_L and the sample size D_2 increased from 6.4 mm to 30 mm, the changes combined increase the beam current by a factor of 88. Generally, a focusing lens allows higher resolution with a shorter instrument when combined with a smaller but higher resolution 2-D detector, which can be inserted in front of the large rear 2-D [27].

To focus the beam, stacks of biconcave refractive spherical lenses are currently in use at multiple facilities [28]. Since the lens focal length $f \propto 1/\lambda^2$, the chromatic aberration is quite large thus limiting the maximum gain. The individual biconcave lens made from MgF_2 single crystal is inexpensive and easy to obtain. Ellipsoidal shaped reflective mirrors eliminate the chromatic aberration thus allowing larger gains and higher q-resolution, as used on the KWS-3 SANS diffractometer [29]. If aligned to reflect vertically, aberration from gravity is also largely eliminated. But the mirror is considerably more expensive and difficult

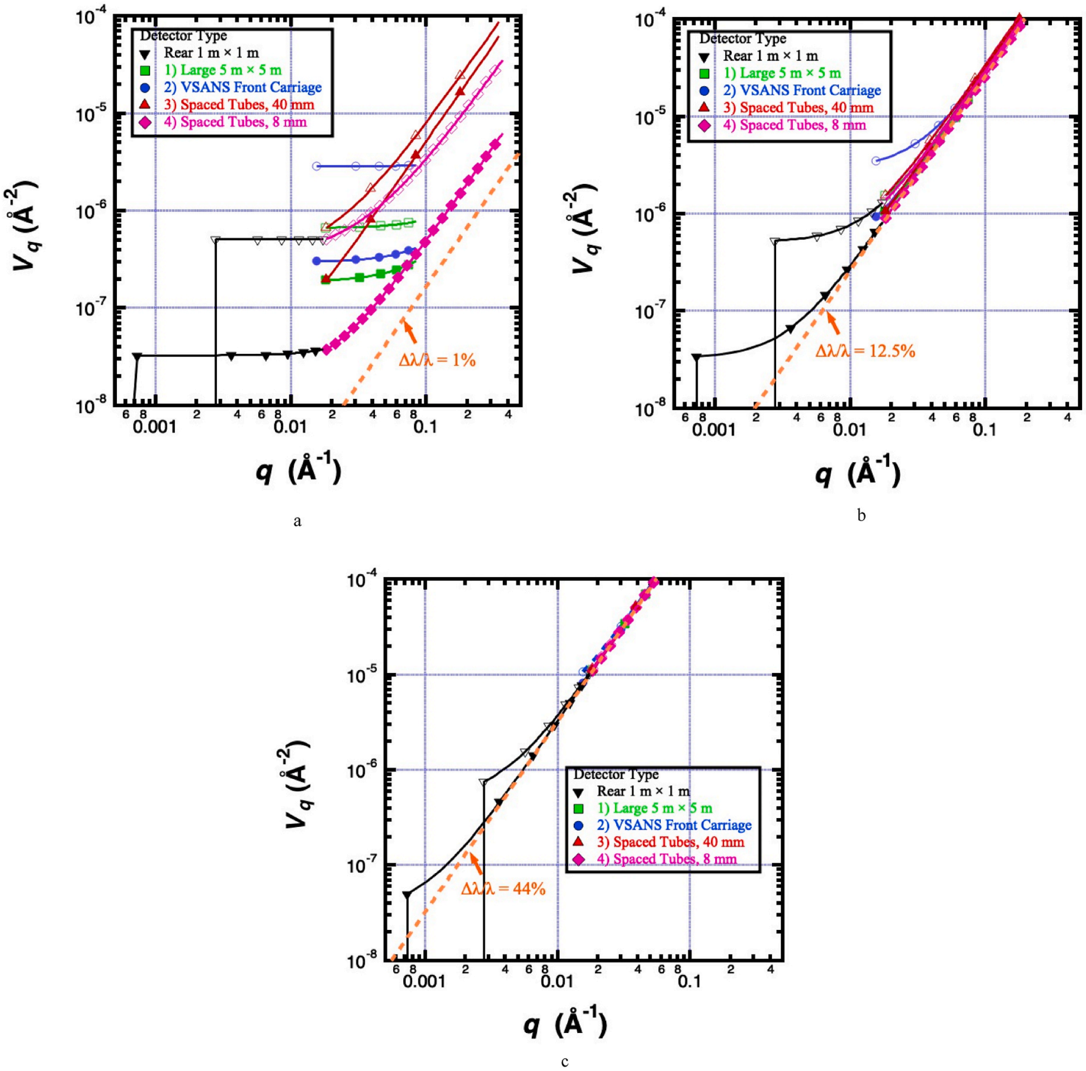

Fig. 7. Plot of variance of the momentum transfer V_q versus q with separate panels for the three different wavelength selection options on the VSANS instrument with a) HOPG $\Delta\lambda/\lambda = 1.0$ %, b) NVS $\Delta\lambda/\lambda = 12.5$ %, and c) deflector $\Delta\lambda/\lambda = 44$ %. The plot combines the four detector options with both a loose and tight collimation. The dashed lines represent only the wavelength component. The total variance is represented by a line and a symbol for every one of ten annuli to avoid clutter, and each annuli being one tube diameter in width. The two collimation choices are described in Table 5 and have beam stop sizes $B_S = 27$ mm (close symbols), and 2) $B_S = 126$ mm (open symbols). Points behind the beam stop are masked. Calculation includes contribution from gravity at $\lambda = 9$ Å.

Table 5
Collimation parameters used to simulate the q-resolution from the different extended-q detector concepts as shown in Fig. 7 using $\lambda = 9$ Å and $\Delta D = 8$ mm for rear detector.

q_L (Å^{-1})	L_1 (m)	L_2 (m)	D_1 (mm)	D_2 (mm)	B_S (mm)	D_{B1} (mm)	D_{B2} (mm)	D_B (mm)	γ	X	Y
7.42×10^{-4}	24.2	20.0	15	6.4	**26.5**	12.4	11.7	24.1	1.1	0.83	0.52
2.47×10^{-3}	21.4	20.0	60	30	**125.7**	56.2	58.1	114.3	1.1	0.94	0.49

to obtain and maintain within performance specifications minimizing both figure error and surface roughness. Similar gains in intensity can be obtained with converging beam collimation [8].

Spallation Sources: The size optimization can also be applied to SANS diffractometers located at spallation neutron sources with some additional considerations. The wavelength band collected using TOF is inversely proportional to the distance from source-to-detector. This restraint provides an additional incentive for shorter instruments at spallation sources. The instrument length or the wavelength bandwidth can be increased by having a lower pulse frequency. Thus, there is an advantage for locating SANS diffractometers at lower pulse frequency sources such as both second target stations at ISIS [30] and Spallation Neutron Source (SNS) [19] and ESS. Choppers are sometimes used to skip every other pulse to half the frequency. Compact moderators at spallation sources can also increase the source brightness. Limiting the source size to 3 cm can increase the brightness by a factor of two at the ESS [31]. The large wavelength band used on TOF SANS diffractometers regardless of the source causes unacceptably large chromatic aberration using refractive optics. A lens using a reflective mirror should be practical.

Short, or compact instruments, particularly suited for spallation sources, are also better optimized for smaller samples. Biological samples are often prohibitively expensive to make in large volumes. Robotic or autonomous activities may also benefit from a smaller sample size [32]. Such an optimized compact instrument for small samples was proposed for the ESS [33], a very bright source which can counter a lower count rate from smaller samples. Whereas this paper has emphasized the gain in count rate from larger samples and instrument components, the same calculations can be used to determine the necessary tradeoffs in performance needed to also shrink the components.

Large Sample Applicability: Both pinhole collimation and lens optics need a larger sample size among other changes to produce an increase in beam current, especially when compared to current instrument design and use. In cases where the increase in sample size can be accommodated and the increase count rate will allow an expansion in the number of samples or sample state variables, such as temperature or pressure, where there are several state conditions to be run, there is incentive for such implementation. Experiments that are particularly suited are experiments that have much lower count rates, make several measurements on the same sample under different state variable conditions, or fast kinetic measurements where individual short time slices have insufficient number of counts. Larger sample sizes are typically currently used on neutron spin echo inelastic scattering instruments, where the same sample must be measured at several solenoid magnetic fields to scan the time variable.

Weak scattering from thin polymer films spin-coated onto large diameter silicon wafers have been measured [34,35]. To enhance the signal, identical films on substrates are stacked together. The background is minimized using vacuum and removing sample area windows. The maximum diameter of the sample is only limited by the available silicon wafer substrates. Kinetic measurements of diffusion in microemulsions have been made, where the signal decays during the diffusion process [36,37]. Faster decay caused by faster diffusion requires higher count rates.

6. Conclusions

Calculations used to optimize the geometry of pinhole SANS diffractometers to maximize detector count rate is revisited, with additional details presented on the penalty paid for using under-sized source or sample apertures. Increasing all instrument component dimensions, which include both source and sample apertures, both path lengths before and after the sample, the beam stop and detector size, produce a gain in detector count rate which scales with the square of all the component's sizes, while maintaining similar q-resolution. The effect of gravity on the q-resolution does grow rapidly with increasing size, but still has a minor influence with current instrument sizes. The performance gain obtained by using larger samples was demonstrated using SANS measurements on the VSANS diffractometer. The versatile detector system, using eight 2-D detector panels mounted on two carriages on rails, allowed the measurements to cover the same q-range, with an observed gain of six in count rate over the typically used sample size.

There are several practical limitations to be able achieve this intensity gain on existing or future SANS diffractometers, with the most difficult being able to maintain or expand the q-range covered in a single measurement. Adding additional detectors closer to the sample with different proposed layouts are shown to be the most practical and cost-effective manner. Sample size availability is another critical factor. To accommodate smaller samples suggest shrinking several instrument dimensions with resulting count rate reduction. Instruments that are flexible in changing size may be the best compromise to handle both small and large samples.

Declaration of competing interest

The authors declare that they have no known competing financial interests or personal relationships that could have appeared to influence the work reported in this paper.

Data availability

Data will be made available on request.

Acknowledgements

The author expresses his thanks to Ryan Murphy, Charlie Glinka and Hubert King for critical reading and comments and Jim Moyer for the tube detector group design drawing. The VSANS instrument is supported in part by the Center for High Resolution Neutron Scattering (CHRNS), a partnership between the National Institute of Standards and Technology and the National Science Foundation, under agreement No. DMR-2010792. All uncertainties in this paper represent one standard deviation.

References

[1] W. Schmatz, T. Springer, J. Schelten, K. Ibel, Neutron small-angle scattering: experimental techniques and applications, J. Appl. Crystallogr. 7 (1974) 96–116.
[2] J.G. Barker, J.C. Cook, Methods to maximize detector count rates on small-angle neutron scattering diffractometers at reactor sources: I. Optimizing wavelength selection, Nucl. Instrum. Methods Phys. Res. (2023) in press.
[3] D.F.R. Mildner, J.M. Carpenter, Optimization of the experimental resolution for small-angle scattering, J. Appl. Crystallogr. 17 (1984) 249–256.
[4] R.P. May, Geometrical optimization of neutron small-angle scattering instruments, J. Appl. Crystallogr. 27 (1994) 298–301.
[5] J.G. Barker, J.S. Pedersen, Instrumental smearing effects in radially symmetric small-angle neutron scattering by numerical and analytical methods, J. Appl. Crystallogr. 28 (1995) 105–114.
[6] C.J. Glinka, J.G. Barker, B. Hammouda, S. Krueger, J.J. Moyer, W.J. Orts, The 30 m small-angle neutron scattering instruments at the national Institute of standards and Technology, J. Appl. Crystallogr. 31 (1998) 430–445.
[7] J.R.D. Copley, The joy of acceptance diagrams, J. Neutron Res. 1 (1993) 21–36.
[8] J. Barker, J. Moyer, S. Kline, G. Jensen, J. Cook, C. Gagnon, E. Kelley, J.P. Chabot, N. Maliszewskyj, C. Parikh, W. Chen, R.P. Murphy, C.J. Glinka, The very small angle neutron scattering instrument at the National Institute of Standards and Technology, J. Appl. Crystallogr. 55 (2022) 271–283.
[9] J.S. Pedersen, D. Posselt, K. Mortensen, Analytical treatment of the resolution function for small-angle scattering, J. Appl. Crystallogr. 23 (1990) 321–333.
[10] A.N. Falcao, J.S. Pedersen, K. Mortensen, Optimum intensity in small-angle neutron scattering. An experimental comparison between symmetric and asymmetric geometries, J. Appl. Crystallogr. 27 (1994) 330–337.
[11] K. Ibel, The neutron small-angle camera D11 at the high-flux reactor, grenoble, J. Appl. Crystallogr. 9 (1976) 296–309.
[12] L. Porcar, D. Pozzo, G. Langenbucher, J. Moyer, P.D. Butler, Rheo-small-angle neutron scattering at the national Institute of standards and Technology center for neutron Research, Rev. Sci. Instrum. 82 (2011), 083902.
[13] C.D. Dewhurst, I. Grillo, D. Honecker, M. Bonnaud, M. Jacques, C. Amrouni, A. Perillo-Marcone, G. Manzin, R. Cubitt, The small-angle neutron scattering instrument D33 at the Institut Laue-Langevin, J. Appl. Crystallogr. 49 (2016) 1–14.
[14] A. Sokolova, A.E. Whitten, L.D. Campo, J. Christoforidis, A. Eltobaji, J. Barnes, F. Darmann, A. Berry, Performance and characteristics of the BILBY time-of-flight small-angle neutron scattering instrument, J. Appl. Crystallogr. 52 (2019) 1–12.
[15] S.R. Kline, Reduction and analysis of SANS and USANS data using IGOR Pro, J. Appl. Crystallogr. 39 (2006) 895–900.
[16] R.K. Heenan, J. Penfold, S.M. King, SANS at pulsed neutron sources: present and future prospects, J. Appl. Crystallogr. 30 (1997) 1140–1147.
[17] S. Takata, J. Suzuki, T. Shinohara, T. Oku, T. Tominaga, K. Ohishi, H. Iwase, T. Nakatani, Y. Inamura, T. Ito, K. Suzuya, K. Aizawa, M. Arai, T. Otomo, M. Sugiyama, The design and q resolution of the small and wide angle neutron scattering instrument (TAIKAN) in J-PARC, JPS Conference Proceedings 8 (2015), 036020.
[18] Y. Noda, H. Izunome, T. Maeda, T. Inada, S. Ueda, S. Koizumi, The large-area detector for small-angle neutron scattering on iMATERIA at J-PARC, Quantum Beam Science 4 (2020) 32.
[19] S. Qian, W. Heller, W.-R. Chen, A. Christianson, C. Do, Y. Wang, J.Y.Y. Lin, T. Huegle, C. Jiang, C. Boone, C. Hart, V. Graves, CENTAUR-The small- and wide-angle neutron scattering diffractometer/spectrometer for the Second Target Station of the Spallation Neutron Source, Rev. Sci. Instrum. 93 (2022), 075104.
[20] S. Jaksch, A. Chenneviere, S. Desert, T. Kozielewski, H. Feilbach, P. Lavie, R. Hanslik, A. Gussen, S. Butterweck, R. Engels, H. Frielinghaus, S. Forster, P. Muller-Buschbaum, Technical specification of the small-angle neutron scattering instrument SKADI at the European spallation source, Appl. Sci. 11 (2021) 3620.

[21] D. Duxbury, R. Heenan, D. McPhail, D. Raspino, N. Rhodes, S. Rogers, E. Schooneveld, E. Spill, A. Terry, Performance characteristics of the new detector array for the SANS2d instrument on the ISIS spallation neutron source, J. Instrum. 9 (2014), C12051.
[22] K.D. Berry, K.M. Bailey, J. Beal, Y. Diawara, L. Funk, J.S. Hicks, A.B. Jones, K. C. Littrell, S.V. Pingali, P.R. Summers, V.S. Urban, D.H. Vandergriff, N.H. Johnson, B.J. Bradley, Characterization of the neutron detector upgrade to the GP-SANS and Bio-SANS instruments at HFIR, Nucl. Instrum. Methods Phys. Res. 693 (2012) 179–185.
[23] R.I. Bewley, J.W. Taylor, S.M. Bennington, LET, a cold neutron multi-disk chopper spectrometer at ISIS, Nucl. Instrum. Methods Phys. Res. 637 (2011) 128–134.
[24] K. Kanaki, A. Jackson, R. Hall-Winton, F. Piscitelli, O. Kirstein, K.H. Andersen, A novel small-angle neutron scattering detector geometry, J. Appl. Crystallogr. 46 (2013) 1031–1037.
[25] J.G. Barker, J.C. Cook, J.P. Chabot, S.R. Kline, Z. Zhang, C. Gagnon, Mitigating background caused by extraneous scattering in small-angle neutron scattering instrument design, J. Appl. Crystallogr. 54 (2021) 461–472.
[26] C.J. Glinka, J.G. Barker, D.F.R. Mildner, Comparison of pinhole collimation and focusing optics for SANS, Nucl. Instrum. Methods Phys. Res. 795 (2015) 122–127.
[27] H. Iwase, H. Endo, M. Katagiri, M. Shibayama, Modernization of the small-angle neutron scattering spectrometer SANS-U by upgrade to a focusing SANS spectrometer, J. Appl. Crystallogr. 33 (2000) 793–796.
[28] S.-M. Choi, J.G. Barker, C.J. Glinka, Y.T. Cheng, P.L. Gammel, Focusing cold neutrons with multiple biconcave lenses for small-angle neutron scattering, J. Appl. Crystallogr. 44 (2011) 558–568.
[29] G. Goerigk, Z. Varga, Comprehensive upgrade of the high-resolution small-angle neutron scattering instrument KWS-3 at FRM II, J. Appl. Crystallogr. 44 (2011) 337–342.
[30] J.W.G. Thomason, The ISIS spallation neutron and Muon source- the first thirty-three years, Nucl. Instrum. Methods Phys. Res. 917 (2019) 61–67.
[31] L. Zanini, K.H. Andersen, K. Batkov, E.B. Klinby, F. Mezei, T. Schonfeldt, A. Takibayev, Design of the cold and thermal neutron moderators for the European Spallation Source, Nucl. Instrum. Methods Phys. Res. 925 (2019) 33–52.
[32] P.A. Beaucage, T.B. Martin, The autonomous formulation laboratory: an open liquid handling platform for formulation discovery using X-ray and neutron scattering, Chem. Mater. 35 (2023) 846–852.
[33] S. Kynde, K.H. Kleno, G. Nagy, K. Mortensen, K. Lefmann, J. Kohlbrecher, L. Arleth, A compact time-of-flight SANS instrument optimised for measurements of small sample volumes at the European Spallation Source, Nucl. Instrum. Methods Phys. Res. 764 (2014) 133–141.
[34] T.P. Russell, P. Lambooy, J.G. Barker, P. Gallagher, S.K. Satija, G.J. Kellogg, A. M. Mayes, Small angle neutron scattering studies on ultrathin films, Macromolecules 28 (1995) 787–789.
[35] R.L. Jones, S.K. Kumar, D.L. Ho, R.M. Briber, T.P. Russell, Chain conformation in ultrathin polymer films using small-angle neutron scattering, Macromolecules 34 (2001) 559–567.
[36] M.H.L. Nguyen, M. DiPasquale, B.W. Rickeard, C.B. Stanley, E.G. Kelley, D. Marquardt, Methanol accelerates dmpc flip-flop and transfer: a SANS study on lipid dynamics, Biophys. J. 116 (2019) 755–759.
[37] Y.-T. Lee, L.D. Pozzo, Contrast-variation time-resolved small-angle neutron scattering analysis of oil-exchange kinetics between oil-water emulsions stabilized by anionic surfactants, Langmuir 35 (2019) 15192–15203.